# Hydrodynamic Analysis of a Suspended Cylinder Under Regular Wave Loading Based on Computational Fluid Dynamics

## Preprint

Philipp Mucha, Amy Robertson, Jason Jonkman, and Fabian Wendt

*National Renewable Energy Laboratory*

*Presented at the 38th International Conference on Ocean, Offshore, and Arctic Engineering*
*Glasgow, Scotland*
*January 9-14, 2019*

**NREL is a national laboratory of the U.S. Department of Energy**
**Office of Energy Efficiency & Renewable Energy**
**Operated by the Alliance for Sustainable Energy, LLC**

This report is available at no cost from the National Renewable Energy Laboratory (NREL) at www.nrel.gov/publications.

Contract No. DE-AC36-08GO28308

**Conference Paper**
NREL/CP-5000-73193
May 2019

# Hydrodynamic Analysis of a Suspended Cylinder Under Regular Wave Loading Based on Computational Fluid Dynamics

## Preprint

Philipp Mucha, Amy Robertson, Jason Jonkman, and Fabian Wendt

*National Renewable Energy Laboratory*

**Suggested Citation**
Mucha, Philipp, Amy Robertson, Jason Jonkman, and Fabian Wendt. *Hydrodynamic Analysis of a Suspended Cylinder Under Regular Wave Loading Based on Computational Fluid Dynamics: Preprint*. Golden, CO: National Renewable Energy Laboratory. NREL/CP-5000-73193. https://www.nrel.gov/docs/fy19osti/73193.pdf.

**NREL is a national laboratory of the U.S. Department of Energy**
**Office of Energy Efficiency & Renewable Energy**
**Operated by the Alliance for Sustainable Energy, LLC**

This report is available at no cost from the National Renewable Energy Laboratory (NREL) at www.nrel.gov/publications.

Contract No. DE-AC36-08GO28308

**Conference Paper**
NREL/CP-5000-73193
May 2019

National Renewable Energy Laboratory
15013 Denver West Parkway
Golden, CO 80401
303-275-3000 • www.nrel.gov

## NOTICE

This work was authored by the National Renewable Energy Laboratory, operated by Alliance for Sustainable Energy, LLC, for the U.S. Department of Energy (DOE) under Contract No. DE-AC36-08GO28308. Funding provided by the U.S. Department of Energy Office of Energy Efficiency and Renewable Energy Wind Energy Technologies Office. The views expressed herein do not necessarily represent the views of the DOE or the U.S. Government. The U.S. Government retains and the publisher, by accepting the article for publication, acknowledges that the U.S. Government retains a nonexclusive, paid-up, irrevocable, worldwide license to publish or reproduce the published form of this work, or allow others to do so, for U.S. Government purposes.



*Cover Photos by Dennis Schroeder: (clockwise, left to right) NREL 51934, NREL 45897, NREL 42160, NREL 45891, NREL 48097, NREL 46526.*

# HYDRODYNAMIC ANALYSIS OF A SUSPENDED CYLINDER UNDER REGULAR WAVE LOADING BASED ON COMPUTATIONAL FLUID DYNAMICS

**Philipp Mucha***
National Renewable Energy Laboratory
Golden, Colorado 80401
Email: philipp.mucha@nrel.gov

**Amy Robertson**
**Jason Jonkman**
**Fabian Wendt**
National Renewable Energy Laboratory
Golden, Colorado, 80401
amy.robertson@nrel.gov
jason.jonkman@nrel.gov
fabian.wendt@nrel.gov

## ABSTRACT

*An investigation into the computation of hydrodynamic loads on a suspended cylinder in regular waves is presented. The primary goal was to perform a three-way validation of the loads between experimental measurements and simulations from two computational methods. Experimental measurements of the longitudinal in-line force on a cylinder suspended at a fixed position were available from the Offshore Code Comparison Collaboration, Continued, with Correlation (OC5) project, Phase Ia. These measurements were compared to computational fluid dynamics (CFD) simulations based on the solution of Reynolds-averaged Navier-Stokes (RANS) equations, as implemented in STAR-CCM+. The study encompassed a sensitivity analysis of the loads computed in STAR-CCM+ based on wave modeling, boundary conditions, turbulence modeling, and spatial and temporal discretization. The analysis was supplemented by results generated with the offshore wind turbine engineering software OpenFAST, based on a hybrid combination of second-order potential flow and viscous drag from Morison's equation. The focus of the investigation was on the assessment of the accuracy of the computation of first- and higher-order hydrodynamic loads. Substantial differences were observed in the numerical prediction of the second and third harmonic force contribution. Local flow field analysis with CFD was applied to study the physics of wave run-up and diffraction dynamics to identify the causes.*

## INTRODUCTION

Simulation-based predictions of hydrodynamic loads on, and motions of, floating structures of offshore wind turbines have increasingly been scrutinized in terms of their accuracy, performance and reliability. The Offshore Code Comparison Collaboration projects OC3, 4 (Continuation), and 5 (Continuation, with Correlation), which operated under the International Energy Agency (IEA) Wind Tasks 23 and 30, sought to verify the accuracy of different simulation methods. Procedures relied on code-to-code comparison (OC3 and OC4) and comparison to experimental data (OC5) for different wave and wind conditions. The goal of the present work was to assess the capability and reliability of a RANS-based CFD method to predict hydrodynamic loading on a suspended cylinder in regular waves. It ties in with the report on OC5 Phase Ia, Robertson et al. [1]. A quintessential finding of OC5 Phase Ia referred to shortcomings of reduced-order wave and hydrodynamic force models concerning nonlinear behavior of both wave dynamics and forces. It was observed that common offshore wind analysis tools failed to accurately capture high-frequency loads arising from the impact of steep wave fronts, with the potential to give rise to transient high-frequency resonant responses (ringing) of the structure, Stans-

*Address all correspondence to this author.

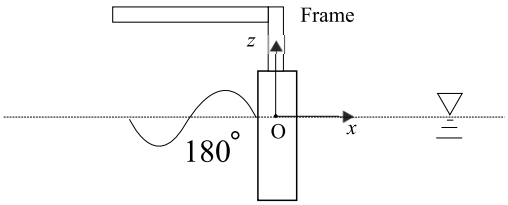


**FIGURE 1**. Coordinate system and model orientation of the suspended cylinder [2]. The right-handed coordinate system originated at the center of the cylinder, or main column, respectively, at the calnwaterline, with positive $x$ being in direction of propagating waves (head waves equivalent to 180 [deg]), and $z$ being up.

berg [2] and Grue and Huseby [3]. For classic papers on this issue refer to Morison et al. [4], Faltinsen et al. [5], Kriebel [6], and Molin [7]. For recent contributions regarding the use of CFD and experimental methods, refer to Kristiansen and Faltinsen [8] and Paulsen et al. [9].

The paper is organized as follows. The description of experimental methods and introduction of test cases is followed by concise outline of the theory behind the computational methods. The discussion of results is split into three parts. First, the modeling of waves in CFD is addressed. Second, computational results are compared to experiments. These sections center on sensitivities of variable parameters and modeling options within CFD and OpenFAST themselves. The ratio of accuracy to modeling and computational cost was evaluated. Third, the analysis of local flow fields available from CFD solutions was used to study the physical effects responsible for the emergence of higher-order forces.

## EXPERIMENTAL METHOD

The validation exercise drew upon the comparison of results from physical experiments conducted with a suspended cylinder, Stansberg [2]. The cylinder with radius $R$=0.38 [m] and draft $d$=1.44 [m] was placed 38.6 [m] downstream of the hydraulic double-flap long-crested wavemaker at one end of the tank, which was 80 [m] in total length, 10.5 [m] in width and was operated at a water depth of 10 [m]. The downstream end of the tank featured a beach designed to absorb incident waves. The tank walls contained wave absorbers. The cylinder was mounted to a stiff carriage and its movement was restricted. The longitudinal force on the cylinder was measured by force transducers. Fig. 1 introduces the relevant coordinate system. Among the many experiments with regular and irregular waves and different cylinder diameters [1], two cases were modeled with CFD, Tab 1.

**TABLE 1**. Parameters of regular wave tests with the suspended cylinder. Water depth is $H$. Wave period is $T$.

| OC5-Ia Test# | $H$ [m] | $T$ [s] |
|---|---|---|
| 8 | 0.37 | 1.533 |
| 14 | 0.45 | 2.114 |

## NUMERICAL METHODS

### Computational Fluid Dynamics

The CFD method drew upon the solution of the RANS equations. The commercial finite volume (FV) method STAR-CCM+ [10] was applied. The fundamentals of finte volume-based methods are abundantly covered in Ferziger and Perić [11]. The transport of turbulent momentum was taken into account by the $k\omega$-SST model [12]. Forces acting upon the structure were obtained by integrating the pressure and shear stresses over the structure's wetted surface. Hexahedral control volumes (CVs) were arranged in an unstructured fashion. A semi-implicit method for pressure linked equations (SIMPLE) algorithm [13] was used for the segregated solution of the velocity-pressure coupling problem. The free-surface was modeled using the Volume of Fluid (VoF) method and a high-resolution interface capturing (HRIC) scheme to achieve tracking of a sharp interface between water and air. An implicit three-level time integration scheme of second order was applied.

Consistent with wave height and water depth regimes encountered in present test cases, regular waves were modeled based on fifth-order Stokes theory for regular waves along the lines of Fenton [14]. Volume fraction and wave velocity components were prescribed at the inlet boundary, which was set two wave lengths $\lambda$ upstream of the coordinate system's origin. The inlet boundary further specified turbulent kinetic energy, turbulent intensity and dissipation rate. The flow field was initialized with the prescribed wave profile in space. A wall boundary condition was set four wavelengths downstream of the reference system which represented the end of a wave damping zone. Modeling the actual dimensions of the experimental tank is expensive from a computational standpoint and can be circumvented by use of a smaller numerical tank including wave damping. Mitigation of wave reflections arising from the downstream boundary of the finite solution domain was achieved through momentum source terms acting on the vertical velocity component $w$ as proposed by Choi and Yoon [15]. Parameters of the model were chosen according to Perić and Abdel-Maksoud [16]: linear damping coefficient $f_1 = \pi\omega$, where $\omega$ is wave frequency and quadratic damping coefficient $f_2 = 0$, and damping zone length $x_d = 2\lambda$ with quadratic ramp exponent $n = 2$.

The bottom boundary was a pressure outlet, with specified hydrostatic pressure according to the present water depth of 10 [m], unity volume fraction for water, a zero-gradient condition

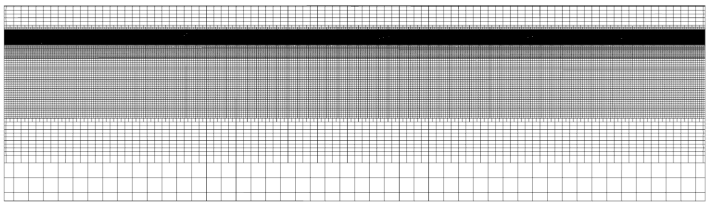

**FIGURE 2**. Side view on the mesh of the numerical tank. Waves with length $\lambda$ propagated from left to right. The damping zone started $2\lambda$ upstream of the outlet.

was inflicted, and velocities were found from the arithmetic average of neighboring cells. This setup was chosen to prevent low-frequency oscillations within the numerical tank arising from potential mass imbalance introduced by the Stokes drift [16], because such a phenomenon were observed for test 8 when the bottom boundary was a wall and the downstream boundary a pressure outlet. The width of the numerical tank equaled the width of the model tank. Free-slip conditions were chosen for the tank side walls. The top boundary was a pressure outlet, with atmospheric pressure and unity volume fraction specified for air. The cylinder represented a no-slip wall and near-wall grid resolution was set up according to the targeted non-dimensional wall distance $y^+ \leq = 1$, where $y^+ = u^\star y/\nu$, and where $u^\star$ is shear velocity at the first CV point from the wall at distance $y$. Kinematic viscosity is $\nu$. Owing to symmetry properties of the cylinder and anticipated symmetry of the flow about the *xz*-plane, a symmetry condition was invoked. The domain extended $0.5\lambda$ into the air phase, seen from the calm waterline.

### OpenFAST

The hydrodynamics module HydroDyn of the computational method OpenFAST for aero-hydro-sevro-elastic simulations of offshore wind turbines was used to compute the hydrodynamic in-line force on the cylinder based on the combination of potential flow theory and Morison's equation; see Jonkman [17]. Linear and second-order wave diffraction forces were computed based on the panel method WAMIT [18], and, in conjunction with the viscous drag term of Morison's equation, constituted the total hydrodynamic force on the constrained body, which was applied at vertically distributed nodes of body members. In this investigation regular waves were generated based on second-order wave theory. The added mass coefficient in Morison's equation was $C_a$=1. The drag coefficient was $C_d$=1.

## RESULTS

### Waves

To ensure an appropriate modeling of waves and to study the effect of discretization on wave dynamics, the numerical tank was setup without the structure present. The governing equations were simplified to cast the dynamics of laminar flow. The wave steepness encountered in the present investigation was 0.0925 (test 8) and 0.056 (test 14) and far from the deep water breaking limit. Furthermore, only one CV extended in the lateral direction, reducing the problem to quasi-2D. The composition of the numerical grid was based on vertical profiles of wave kinematics using layers of different resolution and anisotropic refinement. The resolution around the calm waterline featured 20 CVs across the distance from peak to trough plus an extension of 5% of the wave height in both directions. Grid spacing in the horizontal direction corresponded to 100 CVs per wave length. The mesh was coarsened with increasing distance from the calm waterline. The remaining air phase was discretized by a coarse mesh, as shown in Fig. 2. The so-defined mesh, denoted by medium in the remainder, was coarsened and refined according to $\xi \pm \left(\xi - \xi/\sqrt{2}\right)/2$, where $\xi$ is the length of CV in the *x*- or *z*-direction, respectively. The more common use of a refinement factor like $\sqrt{2}$ resulted in unfavorable discretization levels. The time step was adjusted to keep the Courant-Friedrichs-Lewy (CFL) number constant. For simulations with the medium grid, it corresponded to 500 steps per wave period, which was estimated based on known wave kinematics and grid spacing to ensure that the CFL number would be 0.5 on the free-water surface, according to specified requirements of the HRIC scheme.

Simulations were run on a desktop workstation, and it took 1 hour to simulate 60s of time using the finest level of discretization. Experimental measurements were available for the location corresponding to the position of the cylinder. One hundred and twenty wave probes were distributed across the numerical tank at equidistant locations to record the spatial and temporal resolution of the prescribed waves. The wave heights recorded at each wave probe in the numerical tank, except for those within the damping zone, were averaged over 25 wave periods. This value was used as a metric for the discretization study, as shown in Tables 2 and 3. Figs. 3 and 4 draw the comparison of computed normalized time series of free-surface elevation $\eta$ at the cylinder reference location to experiments for both tests. Figs. 5 and 6 show the comparison to the prescribed theoretical profile and to the experiment over one period for various discretization levels for test 8. The power spectral density (PSD) of entire time signals is compared to the experiment in Fig. 7, and Fig. 8 is a bar plot of the first five peaks of the frequency plot of the normalized absolute Fourier transform. Results confirmed that a coarse resolution in the wave region was not suitable for modeling the prescribed Stokes wave. The deviation to theory was -8%, while the medium and fine grid showed less than $\pm$1%, which pointed to a weak sensitivity to discretization between these points, as shown in Table 2. The frequency analysis comparison showed a prominent under-prediction of the second wave harmonic for the coarse grid. The second harmonic component is approximately

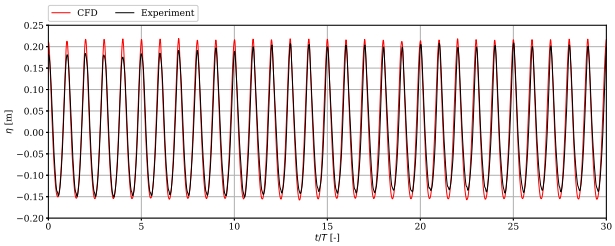


**FIGURE 3**. Comparison of experimental and computational time series of free-surface elevation for test 8, $H$=0.37m, $T$=1.533s, medium grid resolution.

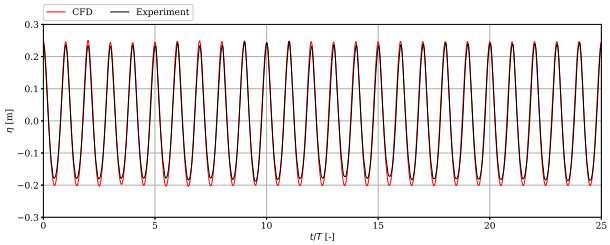


**FIGURE 4**. Comparison of experimental and computational time series of free-surface elevation for test 14, $H$=0.45m, $T$=2.114s, medium grid resolution.

20% of the dominant first-order component. The first three peaks and the fifth peak showed monotonic behavior in the change of magnitude with refined grid and time step. The experimental result percentage difference was -10% compared to theoretical wave height.

The above investigation was also conducted for test 14, Figs. 9 to 12, Table 3. The difference between results of the medium and fine grid was on a similar level than for test 8, while results of the coarse grid were more favorable than for test 8. The deviation to theory was -2% for the medium and fine grid and -4% for the coarse grid. The experimental result percentage difference was -8% compared to theoretical wave height.

In light of observed differences and to establish a better basis for comparison for the load analysis, a least-square regression analysis of the theoretical wave profile of Stokes fifth-order wave and the measurement was performed, where wave elevation and period were chosen as the unknown regressors. Based on so-defined curve fitting, a wave height of 0.3327 [m] and period of 1.536 [s] was found to best approximate the measured wave elevation for test 8, while it was $H$=0.41 [m] and $T$=2.1 [s] for test 14.

## Forces

The introduction of the cylinder to the numerical tank required modification of the computational mesh. The wave region refinement zone was locally extended in the vertical direction such that its top boundary was at a height equivalent to twice the wave amplitude to account for wave run-up. Mesh refinement was also done in the horizontal plane to resolve diffracted waves. Vertical grid spacing was equivalent to the spacing in the global wave region, but the size of CVs in the horizontal plane was decreased by a factor of 1.4. On and adjacent to the body walls prismatic CVs were used and arranged in accordance with the underlying near-wall treatment of the turbulence model. Fig. 13 shows the refinement regions around the cylinder.

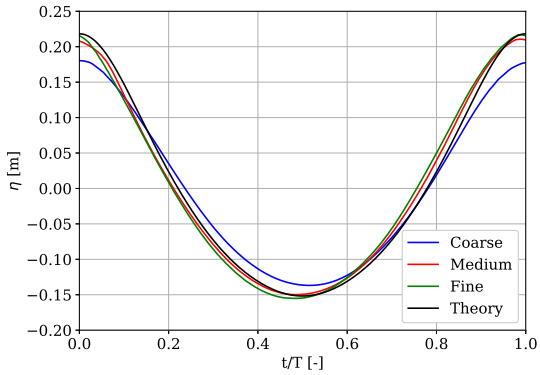


**FIGURE 5**. Sensitivity of free-surface elevation to discretization and comparison to theory, test 8.

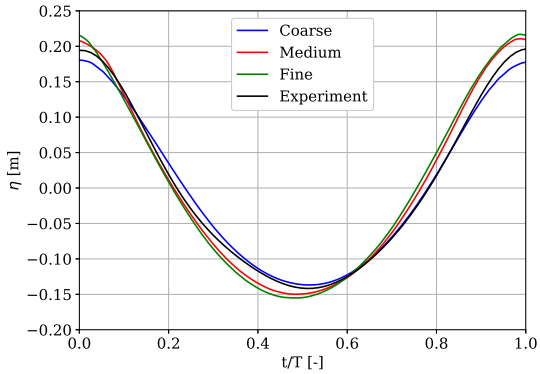


**FIGURE 6**. Sensitivity of free-surface elevation to discretization and comparison to experiment, test 8.

The first part of the discussion is about the comparison of CFD results to measurements, including sensitivity studies on discretization, wave height (calibrated wave), and viscous effects. Second, OpenFAST results are compared to measurements, including a comparison of the combined second-order potential flow with Morison equation, and Morison equation-only method.

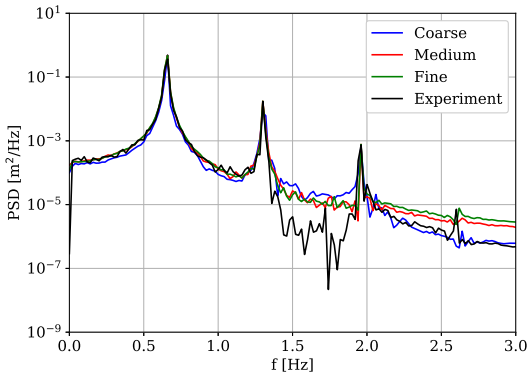


**FIGURE 7**. Sensitivity of power spectral density of free-surface elevation to discretization compared to experiment, test 8.

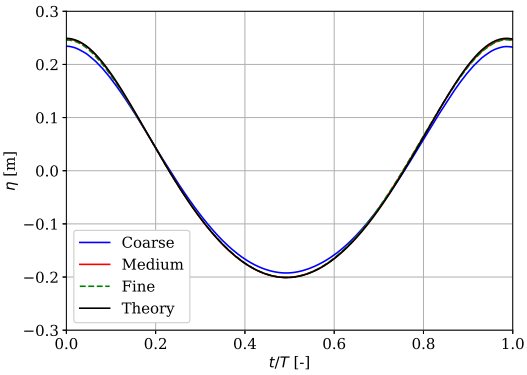


**FIGURE 9**. Sensitivity of free-surface elevation to discretization compared to theory, test 14.

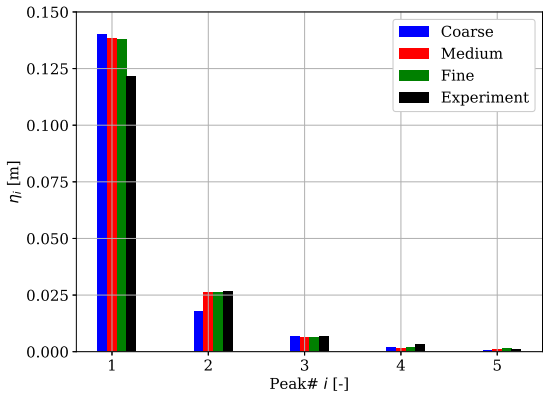


**FIGURE 8**. Sensitivity of wave harmonics of free-surface elevation to discretization compared to experiment, test 8.

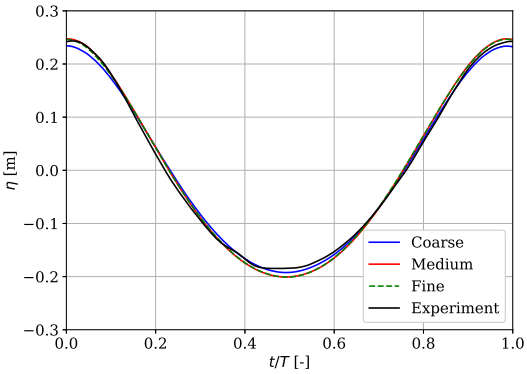


**FIGURE 10**. Sensitivity of free-surface elevation to discretization compared to experiment, test 14.

## Computational Fluid Dynamics

**Sensitivity to discretization** The comparison of the measured longitudinal force to CFD results based on three different levels of discretization was carried out by scrutiny of a representative excerpt from the time series (Figs. 14 and 15), PSD (Figs. 16 and 17) and bar plots related to their peaks (Figs. 18 and 19). The number of CVs ranged from $4.8{\cdot}10^3$ (coarse), to $8.7{\cdot}10^3$ (medium) and $11.3{\cdot}10^3$ (fine). Simulations were run on NREL's high performance computing system and parallelization drew upon $50{\cdot}10^3$ cells per core. The simulation of 60s time took 16 hrs (coarse), 31 hrs (medium), and 46 hrs (fine). Figs. 14 and 15 show that differences between various levels of discretization were again more distinct for test 8. The maximum values of oscillating forces are greater for the finest discretization in test 8, consistent with the findings of the wave-only study. The trend of forces in the range $0 \leq t/T \leq 0.25$ changes with discretization, where the shape of the curve belonging to the finest grid resembled the experimental curve best. For test 14, the sensitivity to discretization was weak and all computational results showed a larger maximum positive force amplitude, consistent with the wave-only study. Figs. 16 and 17 show the PSD of the force signals (unfiltered, 50 [s] time record) from which the non-linearity of the force becomes evident. The quantification of differences between results relied on the comparison of the first three peaks of the normalized absolute Fourier transforms tied to the PSD. The magnitude of the peak at the wave frequencies is ten to twenty times higher than those of the second and third peak. Consequently, the relative comparison errors were more sensitive to deviations. Although the first peak was higher than the experimental value for both test cases, the second peak was always under-predicted. Across the variations of discretization levels, results from the finest level always gave the highest value for all peaks. Except for the second peak of test 8, monotonic

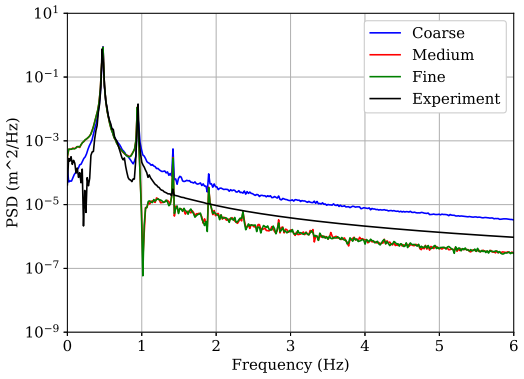


**FIGURE 11**. Sensitivity of power spectral density of free-surface elevation to discretization and comparison to experiment, test 14.

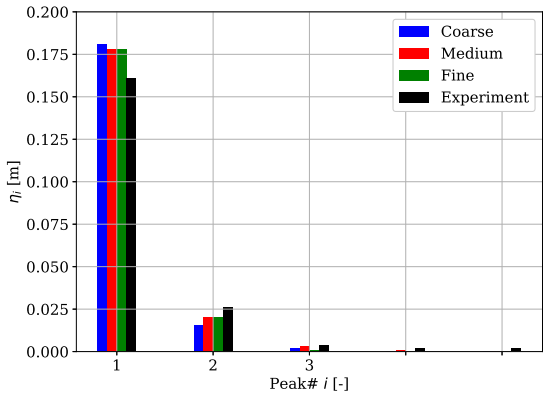


**FIGURE 12**. Sensitivity of wave harmonics of free-surface elevation to discretization and comparison to experiment, test 14.

behavior was observed in results.

Besides the contribution identified in the wave-only study, which mainly affected the first peak, the change of results with changing discretization is attributable to more effects; the integration of pressure and shear over the cylinder surface for different spatial and temporal resolution, and the resolution of wave diffraction in the region ambient to the cylinder. Flow gradients increase with wave steepness. Hence, test 8 showed greater sensitivity to discretization.

**Wave calibration** Computations were run using the finest discretization and prescribing the wave calibrated to match the measured wave based on least-squares regression analysis, Figs. 20 and 21. For both tests, forces decreased. The peak at the wave frequency decreased by approximately 10%, almost proportional to the decrease of prescribed wave heights. The change of the

**TABLE 2**. Monopile: $H$=0.37m, $T$=1.533s, discretization sensitivity study.

| Grid | No of CVs | $\overline{H}$ [m] |
|---|---|---|
| Coarse | 45735 | 0.3410 |
| Medium | 76519 | 0.3697 |
| Fine | 92753 | 0.3730 |
| Theory | - | 0.3700 |
| Experiment | - | 0.3325 |

**TABLE 3**. Monopile: $H$=0.45m, $T$=2.114s, discretization sensitivity study.

| Grid | No of CVs | $\overline{H}$ [m] |
|---|---|---|
| Coarse | 39872 | 0.4285 |
| Medium | 52364 | 0.4411 |
| Fine | 68574 | 0.4404 |
| Theory | - | 0.4500 |
| Experiment | - | 0.4102 |

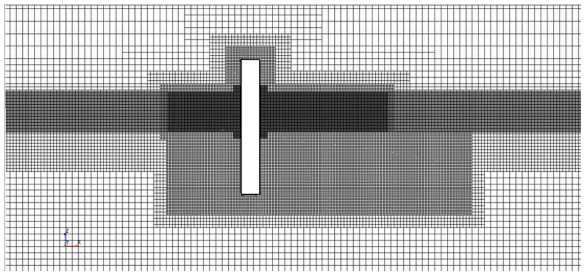

**FIGURE 13**. Side zoom-in view on the mesh around the cylinder.

second and third peak made the agreement with experiments worse for test 8 and the second peak of test 14, but better for the third peak of test 14.

**Viscous effects** In light of the anticipation that the hydrodynamic force on the cylinder is dominated by pressure, rather than shear forces, it was of interest to obtain results based on the solution of Euler equations. For this approach, the computational mesh remained identical, and the fine discretization level was used. Figs. 22 and 23 show the comparison of RANS and Euler equations based computations for the first three peaks including reference to experiments. Test 14 did not show changes in the

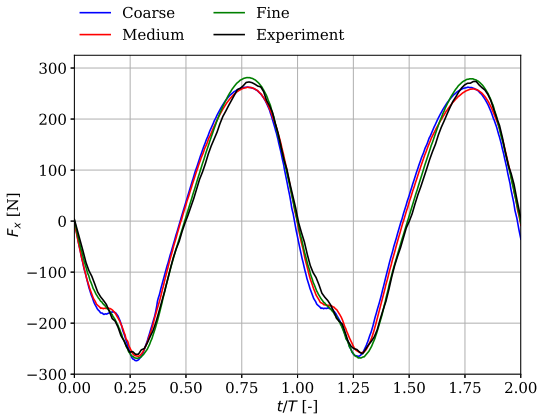


**FIGURE 14**. Sensitivity of longitudinal hydrodynamic force to discretization compared to experiment, test 8.

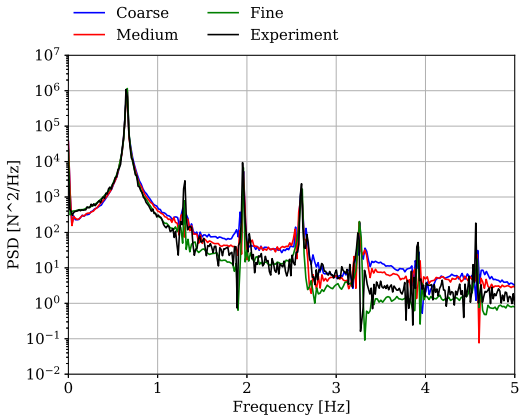


**FIGURE 16**. Sensitivity of power spectral density of the longitudinal hydrodynamic force to discretization compared to experiment, test 8.

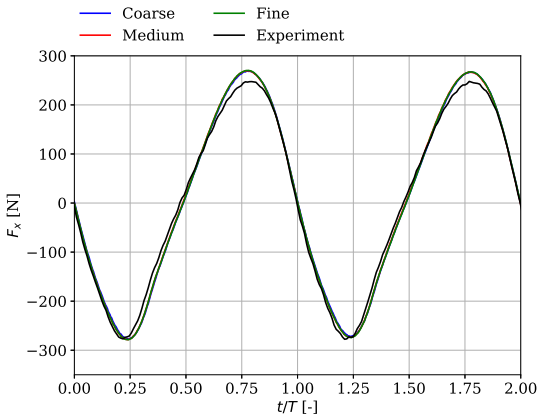


**FIGURE 15**. Sensitivity of longitudinal hydrodynamic force to discretization compared to experiment, test 14.

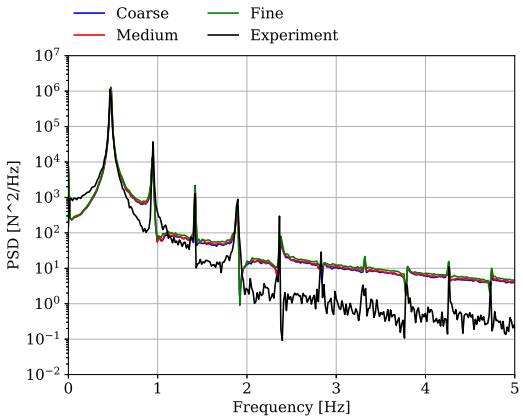


**FIGURE 17**. Sensitivity of power spectral density of the longitudinal hydrodynamic force to discretization compared to experiment, test 14.

first and second harmonic force response; the third peak value was higher than predicted by the RANS method, showing worse agreement with the experimental value. For the steeper wave of test 8, the first peak value differed only slightly (less than 2%), the second peak value almost doubled and the third peak value was 12% higher.

In inviscid flow, the boundary condition on the cylinder inflicts zero normal velocity, while in viscous flow the tangential velocity component is also zero and the surface has a roughness to it. Thus, theoretically the wave run-up on the cylinder will be different and will affect run-up. This in turn will affect the higher-order force harmonics, as wave run-up on the rear side of the cylinder is believed to have an influence on wave diffraction in short and steep waves. Kristiansen and Faltinsen [8] recently showed that if the wave run-up at the rear of the cylinder is prominent and collapses rapidly, it will collapse laterally and give rise to an upstream propagating return wave, which interacts with the incident wave field. The resulting change in the in-line force during the relevant span of the wave period is tied to higher-order force components and reinforces the contributions arising from the presence of higher-order components in the nonlinear wave itself; see Paulsen et al. [9]. Based on idealized large eddy simulation (LES), Kristiansen and Faltinsen [8] demonstrated how viscous effects alter the pressure field in the rear of the cylinder, thereby contributing to the above phenomenon. It should be noted that results of the present investigation represented a general assessment of the relevance of viscous effects, while a more quantitative assessment requires comparison of different modeling approaches to the viscous stress tensor in the Navier-Stokes equations.

**Wave run-up** The process of wave-run up on a cylinder under regular wave loading and its relation to the in-line force is described in the following. Fig. 24 shows the evolution of the in-

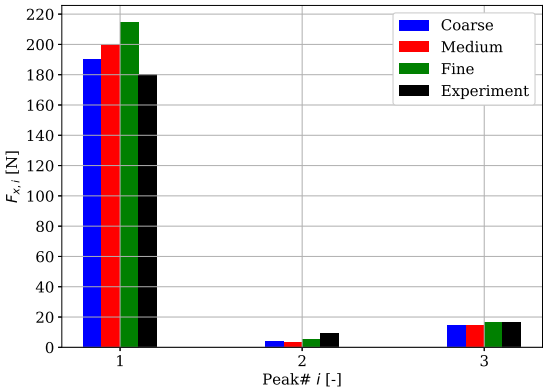


**FIGURE 18**. Bar plot comparison of the three greatest peaks of the longitudinal hydrodynamic force for different levels of discretization, test 8.

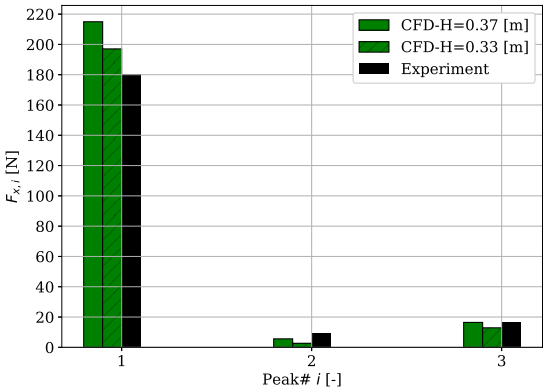


**FIGURE 20**. Comparison of harmonic components of the longitudinal hydrodynamic force between CFD simulations using original and calibrated wave parameters, test 8.

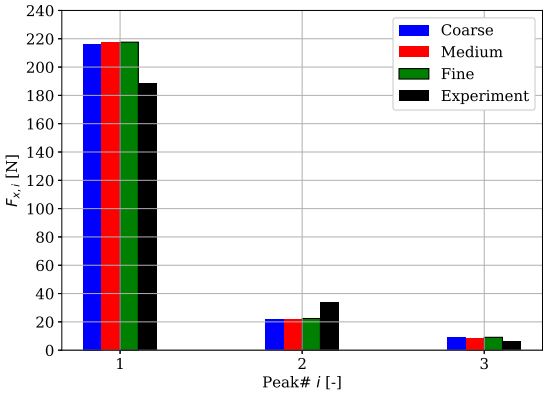


**FIGURE 19**. Bar plot comparison of the three greatest peaks of the longitudinal hydrodynamic force for different levels of discretization, test 14.

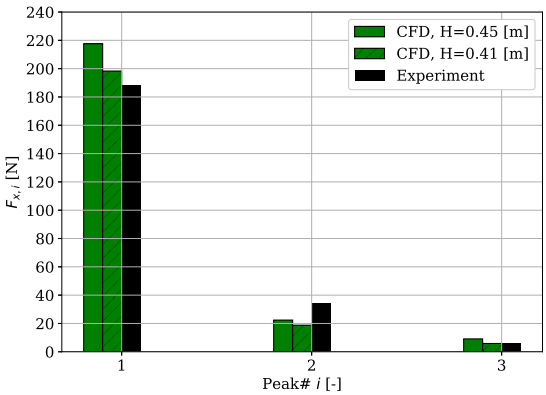


**FIGURE 21**. Comparison of harmonic components of the longitudinal hydrodynamic force between CFD simulations using original and calibrated wave parameters, test 14.

line force from the RANS simulation using the finest discretization level over one wave period, overlaid by the free-surface elevation on the front end (circumferential angle $\Theta$=0°), the rear side (circumferential angle $\Theta$=120°) and the rear end (circumferential angle $\Theta$=180°) over the same time span. The hump in the second half of the period is associated with the so-called secondary load cycle. Along the lines of the analysis presented by Paulsen et al. [9], four time instances were marked and linked to the force and wave run-up time histories. The force was maximum at the time of wave impact (a). The disturbance of the incident wave caused a local run-up at the front of the cylinder, which was maximum shortly after the force had been. After the run-up had reached its maximum at the rear end of the cylinder (b), its collapse lead to aforementioned upstream propagating return wave, which became evident when looking at the free-surface elevation on the side of the cylinder, which saw a secondary increase as the return wave ran through (c). The secondary load cycle ended when the in-line force was minimum (d). The return wave dissipated laterally once it had passed the side of the cylinder and was visible only slightly in the free surface elevation at the front end. The frequency plot of the free-surface elevation at the above locations shows the modification of the different modes compared to the wave harmonics of the undisturbed wave far away from the structure, as shown in Fig. 25. Fig. 26 provides insight into the wave run-up along the circumference of the cylinder at equidistant positions. Fig. 27 is a related scalar plot at aforementioned time instances (left hand side). On the right hand side. the scalar quantity shown is the magnitude of vorticity, which is created by the diffraction of the wave and reinforced by the scattering, especially at the side of the cylinder.

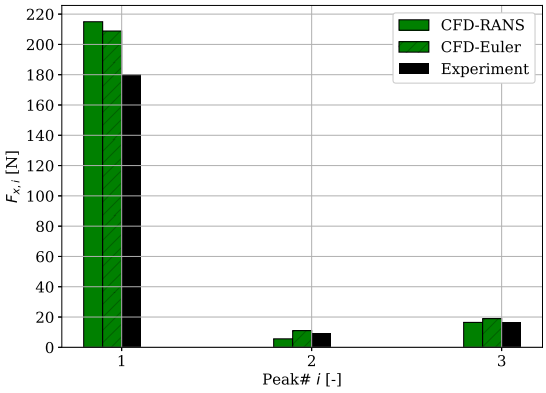


**FIGURE 22**. Comparison of harmonic components of the longitudinal hydrodynamic force between CFD simulations based on the solution of Euler's and RANS equations, test 8.

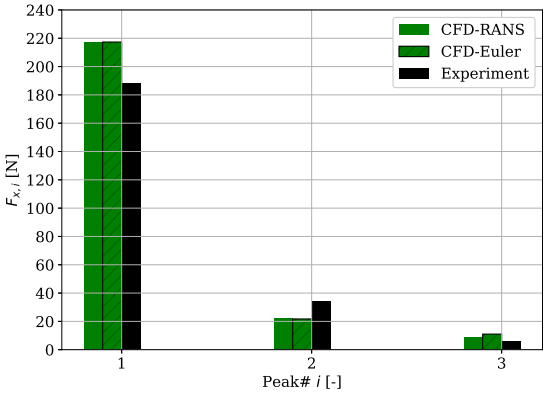


**FIGURE 23**. Comparison of harmonic components of the longitudinal hydrodynamic force between CFD simulations based on the solution of Euler's and RANS equations, test 14.

## OpenFAST

The discussion of results generated with OpenFAST shed light on the computation of forces based on Morison equation and the combination of second-order potential flow with the viscous drag term of Morison equation, where the potential flow solution information stems from application of WAMIT. Analogous to the deviations in wave height encountered between CFD and the experiment, the wave generated by OpenFAST based on the parameters of Table 1 did not agree with the experimental time series. Wave parameters of the underlying wave theory (Stokes second-order) were calibrated in the aforementioned way to establish a better basis for comparison. Time series for both tests 8 and 14 are shown in Figs. 28 and 29; plots of PSD are in Figs. 30 and 31. Results of the potential flow method showed larger values in the first-order force response compared to the

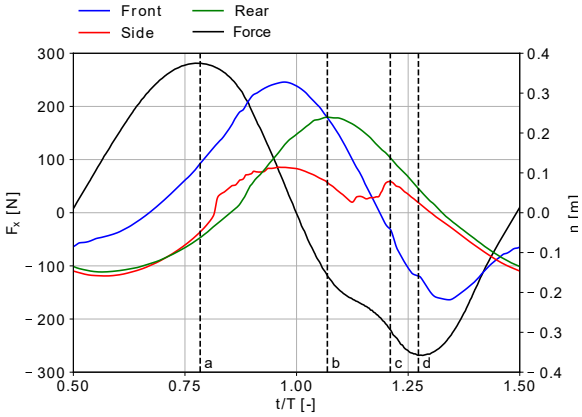


**FIGURE 24**. Comparison of hydrodynamic longitudinal force to free-surface elevation on the front, side, and rear of the cylinder over one wave period. Time instances a) to d) and their significance: a) Force is maximum, wave impact. b) Run-up at rear is maximum, beginning of return flow. c) Beginning of secondary load cycle. d) End of secondary load cycle.

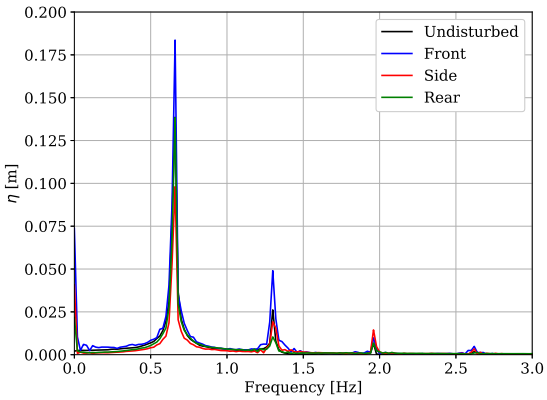


**FIGURE 25**. Frequency plot of free-surface elevation at wave probes on the front, side and rear of the cylinder compared to the undisturbed wave, test 8.

Morison equation method, Figs. 32 and 33. Both methods overpredicted this quantity compared to the experiment. The second peak value is only present for the potential flow model, consistent with the underlying models, higher than the experimental value for test 8, and smaller for test 14. The predicted third-order force contribution is generally small, especially for test 8, but in good agreement between both methods and experiment for test 8.

## Normalized Responses

Given the different wave theories used in the two computational methods on the one hand, and observed differences to the

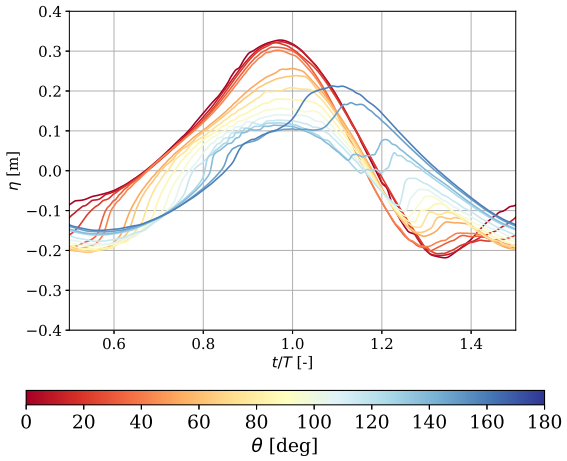


**FIGURE 26**. Comparison of free-surface elevation at wave probes distributed over the circumference of the cylinder over one wave period.

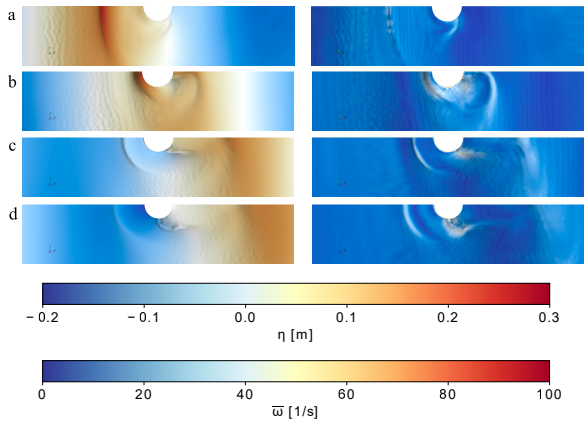


**FIGURE 27**. Scalar plot of free-surface elevation $\eta$ (left) and vorticity magnitude $\overline{\omega}$ (right) at time instances a) to d) introduced in Figure 23.

experimental wave record compared to the specified wave characteristics on the other hand, a final comparison is drawn based on normalized force contributions. The three force harmonics were normalized with the radius of the cylinder squared times the respective wave harmonic at the same frequency raised to the power of the peak. A suitable decimal power was used to establish the comparison. The normalization rules were:

$$\text{Peak 1:} \qquad \acute{F}_1 = \frac{F_1}{10^3 R^2 \eta_1} \tag{1}$$

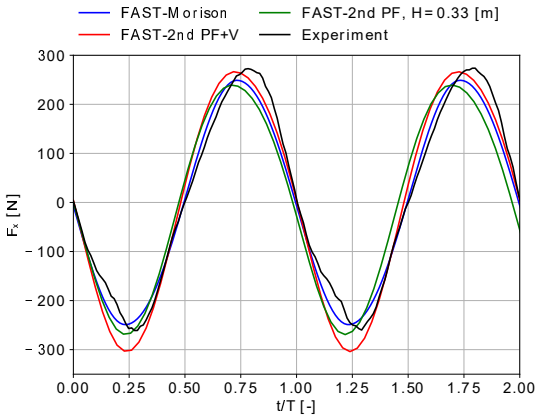


**FIGURE 28**. Comparison of time series of the longitudinal hydrodynamic force between OpenFAST methods 'Morison Equation' and 'Second-order potential flow combined with Morison equation' to experiment, test 8.

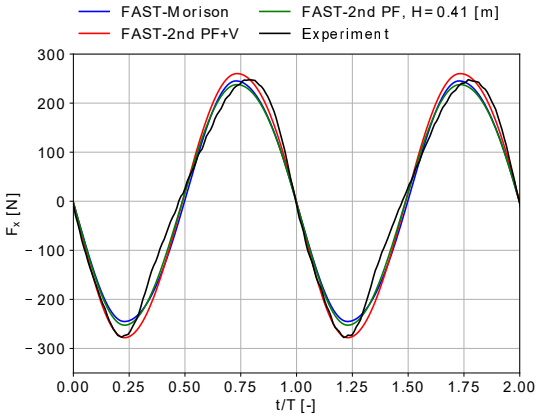


**FIGURE 29**. Comparison of time series of the longitudinal hydrodynamic force between OpenFAST methods 'Morison Equation' and 'second-order potential flow combined with Morison equation' to experiment, test 14.

$$\text{Peak 2:} \qquad \acute{F}_2 = \frac{F_2}{10^5 R^2 \eta_2^2} \tag{2}$$

$$\text{Peak 3:} \qquad \acute{F}_3 = \frac{F_3}{10^9 R^2 \eta_3^3} \tag{3}$$

Results of OpenFAST were excluded from the comparison of the third harmonic, because the respective wave component was zero, which prohibited application of Eq. (1-3). When examined in normalized representation, the agreement of the first peak becomes more favorable for test 8. For test 14, it remained almost

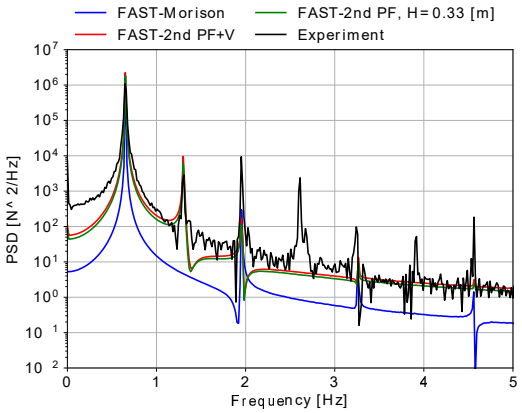


**FIGURE 30**. Comparison of power spectral density of the longitudinal hydrodynamic force between OpenFAST methods 'Morison Equation' and 'second-order potential flow combined with Morison equation' to experiment, test 8.

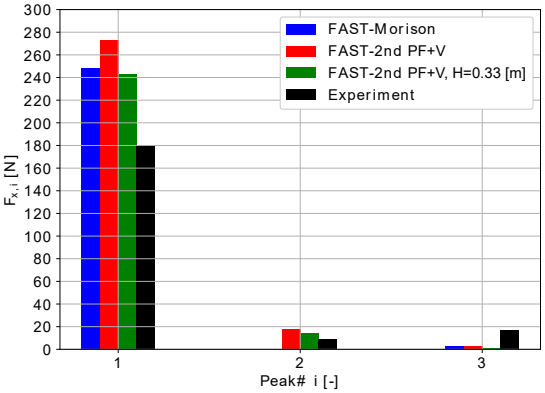


**FIGURE 32**. Comparison of harmonic components of the longitudinal hydrodynamic force between OpenFAST methods 'Morison Equation' and 'second-order potential flow combined with Morison equation' to experiment, test 8.

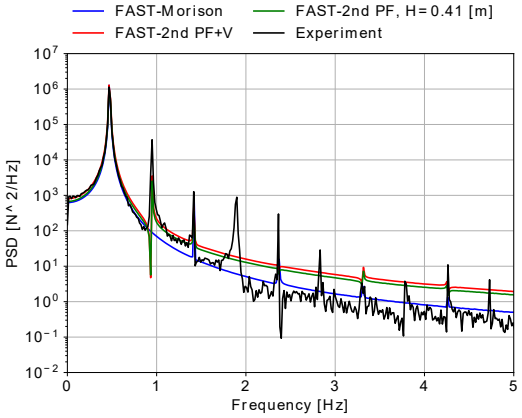


**FIGURE 31**. Comparison of power spectral density of the longitudinal hydrodynamic force between OpenFAST methods 'Morison Equation' and 'second-order potential flow combined with Morison equation' to experiment, test 14.

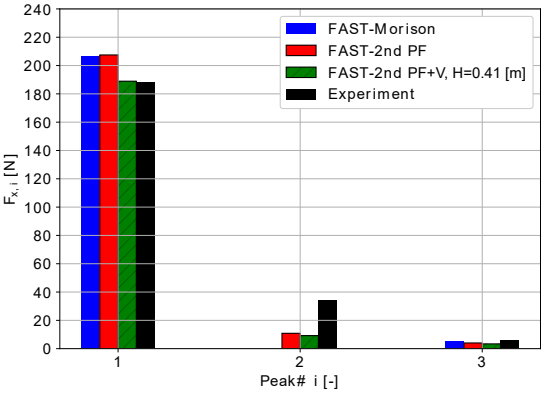


**FIGURE 33**. Comparison of harmonic components of the longitudinal hydrodynamic force between OpenFAST methods 'Morison Equation' and 'Second-order potential flow combined with Morison equation' to experiment, test 14.

the same. The relative comparison errors for the values of the second and third peak were hardly affected by normalization, as shown in Figs. 34 and 35. Results of the finest discretization level in CFD were used.

## CONCLUSIONS

Computations of hydrodynamic loads on a suspended cylinder in regular waves using RANS-based CFD simulations with STAR-CCM+ and OpenFAST were compared to experimental measurements. The focus was on the prediction of higher-order contributions to the loads.

The effort and cost involved in the modeling of waves in CFD was addressed. Accurate resolution of waves required fine discretization in space and time, especially for higher-order regular waves. The preparation of the numerical tank was found to take a substantial share in the overall cost of the application. To study viscous effects, hydrodynamic loads were computed based on Euler equations in addition to the results stemming from the solution of RANS equations.

Application of OpenFAST was less time-consuming and did not require HPC resources, making it attractive for parameter variation studies, even for the most sophisticated available model within OpenFAST based on second-order potential flow, given available hydrodynamic characteristics from WAMIT. Consistent with expectations, the hybrid method based on second-order

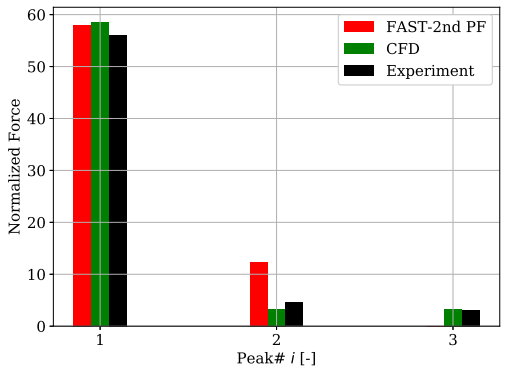


**FIGURE 34**. Comparison of normalized harmonic components of the longitudinal hydrodynamic force between CFD, OpenFAST and experiment. Normalization based on wave harmonics derived for each single method, test 8.

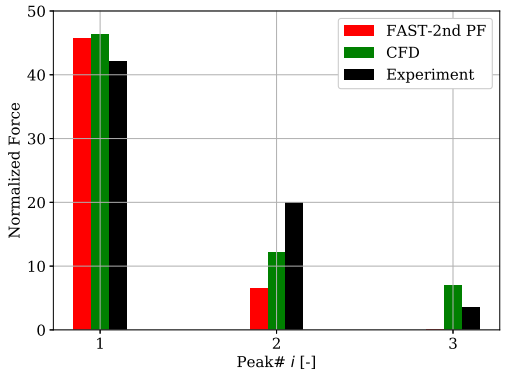


**FIGURE 35**. Comparison of normalized harmonic components of the longitudinal hydrodynamic force between CFD, OpenFAST and experiment. Normalization based on wave harmonics derived for each single method, test 14.

potential flow and Morison's equation gave the best results for OpenFAST as compared to solving Morison equation only. In this method, the diffraction force is simplified based on the long wavelength approximation and tied to the inertia force term. The third-order contribution stems from the nonlinear drag term. The magnitude of these force contributions are essentially tied to the hydrodynamic inertia and drag coefficients, which fail to account for the anticipated complexity of nonlinear wave diffraction.

Time series of free surface elevation and in-line forces were compared to experimental measurements. Favorable agreement was observed for first-order load contributions across all methods and variations within these methods. Substantial differences were observed in the numerical prediction of the second and third harmonic force contribution. Local flow field analysis with CFD was applied to study the physics of wave run-up and diffraction dynamics to identify the causes for the observed differences. Nonlinear dynamics of the free surface are inherently captured by the CFD method. However, higher-order diffraction dynamics were linked to the run-up and collapse of the wave on the rear of the cylinder, the accurate prediction of which is sensitive to the computation of pressure in this region. Simplifications inflicted by the Reynolds-averaging of the Navier-Stokes equations and two-equation eddy viscosity models are assumed to introduce modeling errors in the prediction of the flow field in the rear of the cylinder. Recent research into viscous effects and turbulence modeling relevant to this problem supported this assumption [8]. Measurements of wave run-up and sensitivity analysis with respect to turbulence modeling are considered a requirement to provide final evidence for this hypothesis.

## ACKNOWLEDGMENT

This work was authored by Alliance for Sustainable Energy, LLC, the manager and operator of the National Renewable Energy Laboratory for the U.S. Department of Energy (DOE) under Contract No. DE-AC36-08GO28308. Funding was provided by the DOE Office of Energy Efficiency and Renewable Energy, Wind Energy Technologies Office. The views expressed in the article do not necessarily represent the views of the DOE or the U.S. Government. The U.S. Government retains and the publisher, by accepting the article for publication, acknowledges that the U.S. Government retains a nonexclusive, paid-up, irrevocable, worldwide license to publish or reproduce the published form of this work, or allow others to do so, for U.S. Government purposes.

## REFERENCES

[1] Robertson, A., Wendt, F., Jonkman, J., Popko, W., Vorpahl, F., Stansberg, C, Bachynski, E., Bayati, I., Beyer, F., de Vaal, J.B., Harries, R., Yamaguchi, A., Shin, H., Kim, B., van der Zee, T, Bozonnet, P., Aguilo, B., Bergua, R., Qvist, J., Qijun, W., Chen, X., Guerinel, M., Tu, Y., Yutong, H., Li, R., Bouy, L. *2015 OC5 Project Phase I: Validation of Hydrodynamic Loading on a Fixed Cylinder* Proceedings of the International Offshore and Polar Engineering Conference (ISOPE 2015), Kona, Hawaii

[2] Stansberg, C.T., Krokstad, J.R.; and Lehn, E. *1995 Experimental Study on Non-Linear Loads on Vertical Cylinders in Steep Random Waves* Proceedings of the Fifth International Offshore and Polar Engineering Conference

[3] Grue, J., Huseby, M. *2005 Higher-harmonic wave forces and ringing of vertical cylinders* Applied Ocean Research, 24(4):203-214

[4] Morison, J. R., O'Brien, M. P., Johnson, J. W., Schaaf,

S. A. *1950 The force exerted by surface waves on piles* Petroleum Transactions (American Inst. of Mining Engineers) 189, 149–154

[5] Faltinsen O. M., Newman J. N., Vinje T. *1995 Nonlinear wave loads on a slender vertical cylinder* Journal of Fluid Mechanics, 289:179-198

[6] Kriebel, D.L. *1992 Nonlinear Wave Interaction with a Vertical Circular Cylinder. Part II: Wave Run-Up* Ocean Engineering 19(1):75-99

[7] Molin, B. *1979 Second-order Diffraction Loads Upon Three-Dimensional Bodies* Applied Ocean Research 1:197-202

[8] Kristiansen, T., Faltinsen, O.M. *2017 Higher harmonic wave loads on a vertical cylinder in finite water depth* Journal of Fluid Mechanics 883:773-805

[9] Paulsen, B.T., Bredmose, H., Bingham, H.B., Jacobsen, N.G. *2014 Forcing of a bottom-mounted circular cylinder by steep regular water waves at finite depth* Journal of Fluid Mechanics 755:1-34

[10] Siemens PLM Software *2018 Simcenter STAR-CCM+ User Guide* Version 13.02.013

[11] Ferziger, J., Perić, M. *2002, Computational Methods for Fluid Dynamics* Springer

[12] Menter, F.R. *1994 Two-Equation Eddy-Viscosity Turbulence Models for Engineering Applications* AIAA Journal, Vol. 32, No. 8, pp. 1598-1605

[13] Caretto, L.S., Gosman, A.D., Patankar, S.V., and Spalding, D.B. *1972 Two calculation procedures for steady, three-dimensional flows with recirculation* Proc. of the 3rd International Conference on Numerical Methods Fluid Dynamics

[14] Fenton, J. D. *1985. A fifth-order stokes theory for steady waves* Journal of Waterway, Port, Coastal, and Ocean Engineering 111(2):216-234

[15] Choi, J. and Yoon, S. B. *2009 Numerical simulations using momentum source wave-maker applied to RANS equation model* Coastal Engineering 56(10):1043–60

[16] Perić, R., Abdel-Maksoud, M. *2016 Reliable damping of free-surface waves in numerical simulations* Ship Technology Research 63(1):1-13

[17] Jonkman, J., OpenFAST User Manual, Available from https://nwtc.nrel.gov/OpenFAST, called 11-01-2018

[18] Wamit, Inc. WAMIT User Manual, Version 6.4s, WAMIT Inc.: Chestnut Hill, 200X. (Available from www.wamit.com), called 11-01-2018